Improvements in the properties of low-Ag SAC105 solder alloys with the addition of tellurium

Panisara Sukhontapatipak[1] and Phairote Sungkhaphaitoon[1,*] (ORCID)

[1] *Materials Science Program, Division of Physical Science, Faculty of Science, Prince of Songkla University (PSU), Hat Yai, Songkhla 90110, Thailand*

ABSTRACT

Tellurium (Te) was added to SAC105 solder alloy to improve various properties. The effects of Te on the microstructure, melting behavior, mechanical properties, and wettability of the solder alloy were studied. The microstructure of SAC105 solder included a primary β-Sn phase and Ag_3Sn and Cu_6Sn_5 IMC phases. The addition of Te led to the formation of a SnTe IMC phase in the solder matrix and coarsened the β-Sn phase and IMC phases. Te slightly affected the melting temperature and pasty range but increased the undercooling of the solder alloy. Adding Te to SAC105 solder increased yield strength (YS), ultimate tensile strength (UTS), and hardness due to the second-phase strengthening effect, but adding more than 0.5 wt.% Te reduced both YS and UTS due to coarsening of the microstructure. The fracture surface of SAC105 solder indicated a ductile fracture mode, but a mixed ductile–brittle fracture mode developed with increments of added Te. Te improved the wettability of the solder alloy, but the thickness of IMC layers was not significantly changed by Te content. Our findings suggested that 0.5 wt.% Te was the optimal amount to add to SAC105 solder.

1 Introduction

Solder alloys are important materials for the fabrication of integrated circuits and electronic devices. Lead-containing solders such as Sn–Pb solder are popular because of their low melting point, superior solderability, and low price. However, when electronic devices are discarded, the hazardous lead in the used solder poses a threat to both human health and the environment [1]. Therefore, Pb-based solder alloys have been replaced by more recently developed lead-free solder alloys such as Sn–Cu [2], Sn–Bi [3], Sn–Ag [4], Sn–Ag–Cu [5], Sn–Cu–Ni [6], Sn–Ag–Cu–Zn [7], and Sn–Sb [8]. The Sn–Ag–Cu (SAC) solder group has been widely applied, particularly SAC solder alloys with Ag contents ≥ 3 wt.%, such as Sn–3.0Ag–0.5Cu (SAC305). These solder alloys have high mechanical strength, good solderability and perform well at higher temperatures but do present some disadvantages. Since SAC305 solder has a higher melting point than Sn–Pb solder, coarse Ag_3Sn intermetallic compound (IMC) phases can

Address correspondence to E-mail: phairote.s@psu.ac.th

form during soldering. IMCs can weaken solder joints, and the reliability of joints can be reduced by the growth of IMC layers along the solder–pad interface during soldering [9, 10]. Also, the cost of the high Ag content in SAC305 solder has become a big issue in industrial solder production, prompting the development in recent years of cheaper SAC solder alloys with Ag content < 2 wt.%. Solder alloys such as Sn–0.3Ag–0.7Cu (SAC0307) and Sn–1.0Ag–0.5Cu (SAC105) have come to the fore but some properties of these newly developed lead-free solders are not as good as the same properties of Sn–Pb solder alloys. Their melting points are higher, wettability lower, and they have weak fatigue properties [11–14]. These shortcomings of low-Ag solders can be improved by the minor addition of other elements to resolve the issues they cause. For example, Chen et al. [12] added Bi to SAC105 solder alloy. They found that Bi decreased the thickness of the IMC layer that formed between the solder and substrate and increased shear strength. The reliability of the SAC105 solder joints was significantly improved. Mahdavifard et al. [15] found that the ultimate tensile strength (UTS), yield strength (YS), and total elongation of SAC105 solder with additions of Fe and Bi did not change after aging treatment. Bi inhibited chemical reactivity between Sn and Cu or Sn and Ag, reducing the formation of Cu_6Sn_5 and Ag_3Sn IMC phases. Furthermore, Fe atoms partially dissolved in the Cu_6Sn_5 phase, reducing the coarsening of the microstructure. The hardness of the SAC105 solder was also increased. El-Daly et al. [16] reported that the addition of Ni and Sb to an SAC105 solder reduced undercooling, increased the eutectic area, and enlarged the volume of the proeutectic fraction. The refined dendritic size and improved creep resistance extended the lifetime of the solder joint. El-Daly et al. [17, 18] reported that the addition of Te and Co to Sn-1.7Ag-0.7Cu (SAC177) solder refined the Ag_3Sn, and Cu_6Sn_5 IMC phases and led to the formation of $(Cu, Co)_6Sn_5$ and Co_3Sn particles. Te reacted with Sn to form new hexagonal SnTe particles within the eutectic and dendritic regions of the solder. The SnTe phase hindered the growth of Cu_6Sn_5 and Cu_3Sn IMCs at the interface between solder and substrate by reducing the driving force. Hence, the Te and Co microalloying elements increased the mechanical properties and microelectronic reliability of the SAC177 solder.

A review of the literature showed that minor additions of certain elements can improve properties and modify the microstructure of low Ag-content solder alloys. This research presents studies of the effects of Te on the microstructure and thermal and mechanical properties of SAC105 solder alloys. The solder alloys were jointed with a copper substrate to evaluate wetting properties such as the spreading area and contact angle of the solder joints.

2 Experimental procedure

2.1 Sample preparation

The solder alloys were prepared in four different compositions: Sn–1.0Ag–0.5Cu (SAC105), Sn–1.0Ag–0.5Cu–0.5Te (SAC105-0.5Te), Sn–1.0Ag–0.5Cu–1.0Te (SAC105-1.0Te), and Sn–1.0Ag–0.5Cu–1.5Te (SAC105-1.5Te). High-purity (99.95 wt.%) Sn, Ag, Cu, and Te ingots were melted in an electric furnace at 400 °C for 4 h under ambient conditions. The liquid solder was then homogenized by mechanical stirring. Prior to casting, the melt temperature was lowered to 250 °C to prevent oxidation and a steel mold was preheated to 200 °C to prevent the melt solidifying during casting. The alloy was then poured into the heated steel mold and allowed to cool naturally to room temperature. For tensile testing, samples were machined according to ASTM E8 standards. To prepare the alloys for the soldering process, ingots of the as-cast alloy were rolled to a thickness of 3 mm and then compressed using a hydraulic press to create solder wire with a diameter of 3 mm. Copper pads with dimensions of 25.4 mm × 25.4 mm × 0.3 mm were used as the substrate, and before use were abraded using SiC papers, submerged in diluted HCl for 30 min, rinsed with ethanol, and dried using an air blower.

2.2 Sample characterization

Before microstructural observation, samples underwent metallographic preparation. The microstructure was observed by scanning electron microscopy (SEM, Hitachi, SU3900). Phase identification was performed using energy dispersive X-ray spectroscopy (EDS, Oxford, X-Max^{N}20) and X-ray diffraction analysis (XRD, PANalytical Empyrean). The thermal characteristics of solder alloys were analysed using a differential scanning calorimeter (DSC, NETZSCH, DSC 200 F3 Maia). Samples were heated and cooled from

30 °C to 300 °C in a nitrogen atmosphere at heating and cooling rates of 10 °C/min to produce heating and cooling curves. Tensile tests were conducted on a universal testing machine (UTM, Instron 5569) at a constant strain rate of 1.5 mm/min at room temperature. Three test results were averaged to determine

Fig. 1 Illustration of the spreading test setup

tensile strength values. The average microhardness of solder alloys was determined using the Vickers microhardness test (INNOVATEST, NOVA 130/240) at a load of 200 g and a dwell time of 10 s. The spreading of solder alloys was investigated using the sessile drop (SD) method [19] on a Cu substrate. In this procedure, the solder wire was placed on a Cu substrate with a small amount of rosin mildly activated (RMA) flux. The sample was then placed on a heating plate, heated to 250 °C, held for 2 min, then removed from the heating plate and allowed to cool to room temperature. Samples received after the spreading tests were called reflowed samples (Fig. 1) and were used to measure contact angles and spreading areas according to the Japanese Industrial Standard JIS-Z3198-3 [20]. The wettabilty of each tested solder alloy was reported as the average of
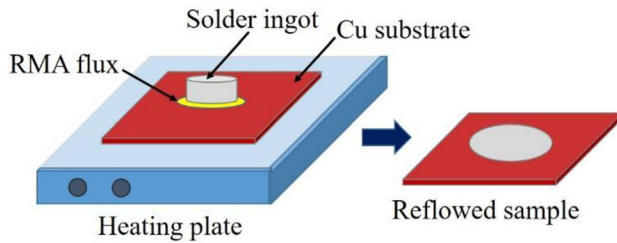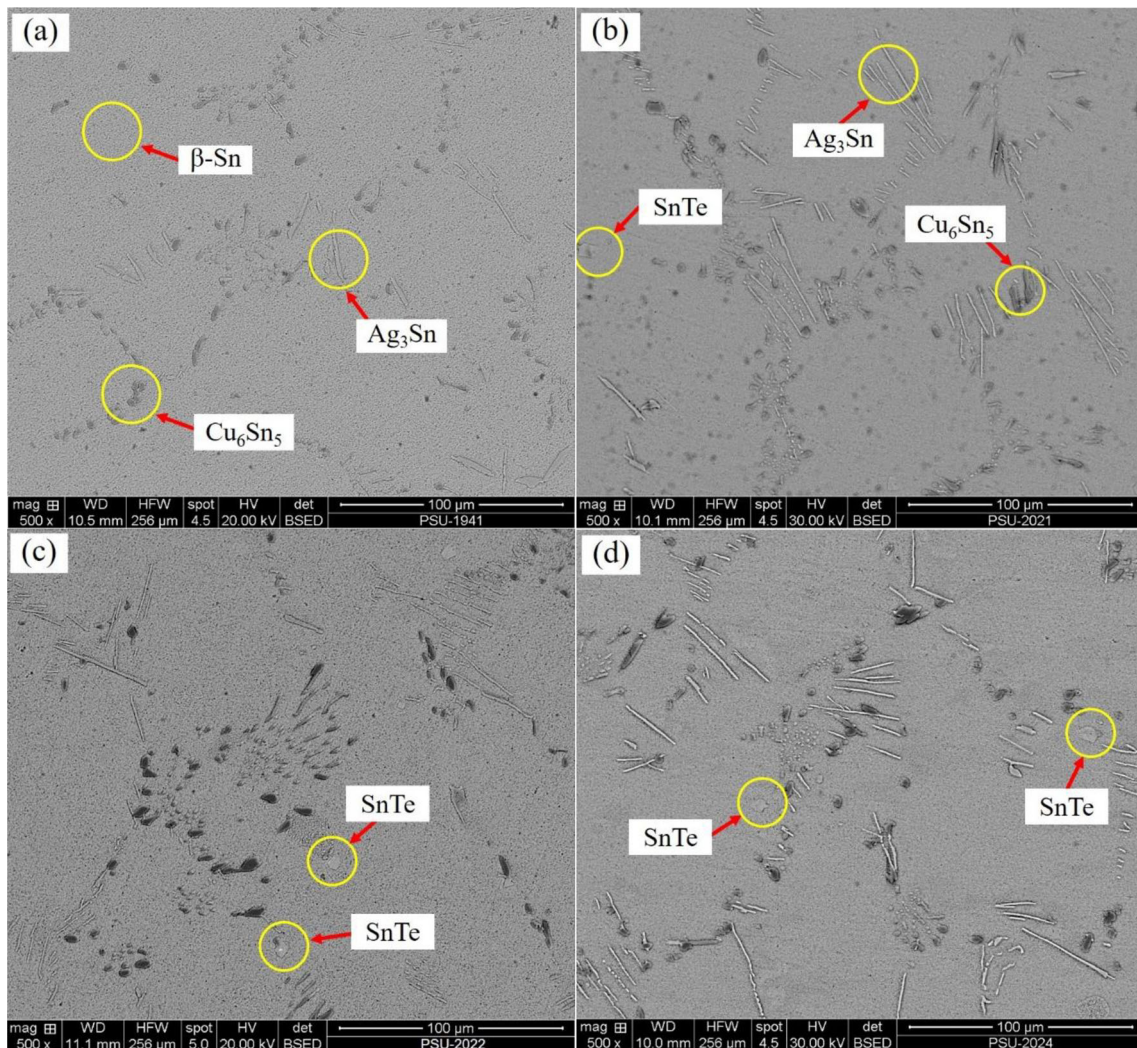

Fig. 2 SEM micrographs are of **a** SAC105, **b** SAC105-0.5Te, **c** SAC105-1.0Te, and **d** SAC105-1.5Te solder alloys
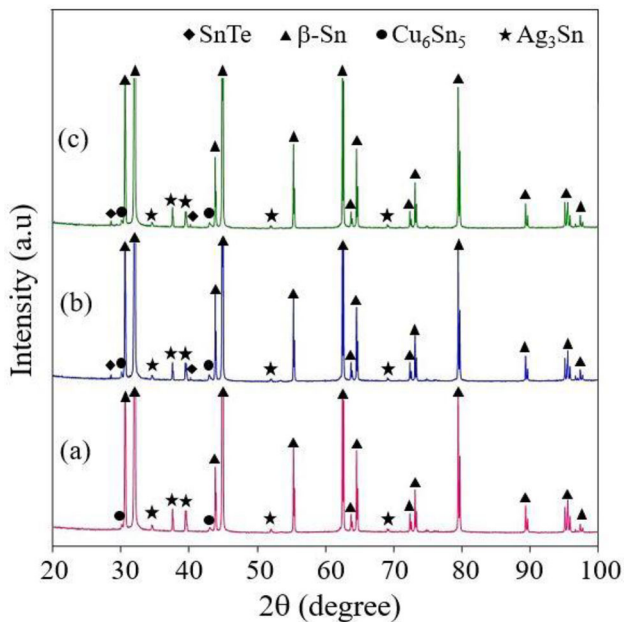
Fig. 3 XRD patterns were produced by **a** SAC105, **b** SAC105-0.5Te, and **c** SAC105-1.5Te solder alloys

three samples. For microstructure observation and evaluation of the interfacial layer between solder and Cu substrate, reflowed samples were cut perpendicular to the plane of the interface, mounted in epoxy resin, and polished.

3 Results and discussion

3.1 Microstructure observation

The microstructures in the SAC105 base solder consisted of needle-like Ag_3Sn IMCs and globular particles of Cu_6Sn_5 IMCs within a β-Sn matrix (Fig. 2a) [14–16]. The solder alloys containing Te presented SnTe IMC particles within the eutectic area, and the number of SnTe IMC particles formed increased with increments of Te content (Fig. 2b–d). Sn and Te atoms could react in the liquid state to form SnTe. The nucleation rate of SnTe increased when the temperature was reduced, which promoted the development of SnTe IMC particles [17, 18]. The XRD study supported the SEM observations of IMC phases in the solder alloys. The XRD pattern of the SAC105 base solder showed mostly strong peaks attributed to the β-Sn phase and small peaks attributed to Cu_6Sn_5 and Ag_3Sn IMC phases (Fig. 3a). SnTe IMC phases within the solder matrix were represented by small peaks at

approximately 28–40° 2θ in the XRD patterns of SAC105-0.5 and SAC105-1.5 solder alloys (Fig. 3b, c). The phase compositions of SAC105 and SAC105-1.5Te solder alloys (Fig. 4a and b) were identified by EDS analysis. Only Ag_3Sn and Cu_6Sn_5 IMC phases were detected in the solder matrix of the SAC105 solder. Their respective compositions were 71.0 at% Ag and 29.0 at% Sn (Fig. 4c spectrum 1), and 51.1 at% Cu and 48.9 at% Sn (Fig. 4d spectrum 2). The SAC105-1.5Te solder presented Cu_6Sn_5, SnTe, and Ag_3Sn IMC phases in the solder matrix. The compositions of these phases were 37.7 at% Cu and 62.3 at% Sn (Fig. 4e spectrum 3), 56.7 at% Sn and 43.3 at% Te (Fig. 4f spectrum 4), and 47.2 at% Sn, 51.9 at% Ag, and 0.9 at% Te (Fig. 4g spectrum 5). The phase compositions of the solder alloys were summarized in Table 1.

3.2 Thermal analysis

Thermal analysis using DSC revealed the thermal behavior of the SAC105, SAC105-0.5Te, SAC105-1.0Te, and SAC105-1.5Te solder alloys. The DSC heating curves of all the solder alloys displayed two endothermic peaks (Fig. 5a–d). The first peak indicated the eutectic temperature, and the second peak the melting point of the primary β-Sn phase [16, 21]. The addition of Te slightly affected the melting behavior of the SAC105 solder. These results were consistent with reports of SAC177-0.2Te solder by El-Daly et al. [18]. According to Li et al. [22], solder alloys should have a small pasty range that does not exceed 30 °C. Since the SAC105-0.5Te, SAC105-1.0Te, and SAC105-1.5Te solder alloys had pasty ranges of 11.3 to 12.7 °C, they could be used under the same circumstances as the conventional SAC105 alloy. The solidification behavior of solder alloys is affected by the degree of undercooling, defined by T_{onset} heating minus T_{onset} cooling. The addition of Te significantly increased the degree of undercooling of the solder alloy. The undercooling of the SAC105 solder was 11.5 °C, while the undercoolings of the SAC105-0.5Te, SAC105-1.0Te, and SAC105-1.5Te alloys were 12.6, 17.4, and 20.1 °C, respectively (Table 2). Increased undercooling was reported to hinder nucleation of the β-Sn phase during solidification of Pb-free Sn-based solder alloys [13, 23]. Therefore, in the present study, due to their greater amounts of undercooling, the alloys containing Te produced larger primary β-Sn grains compared to the SAC105
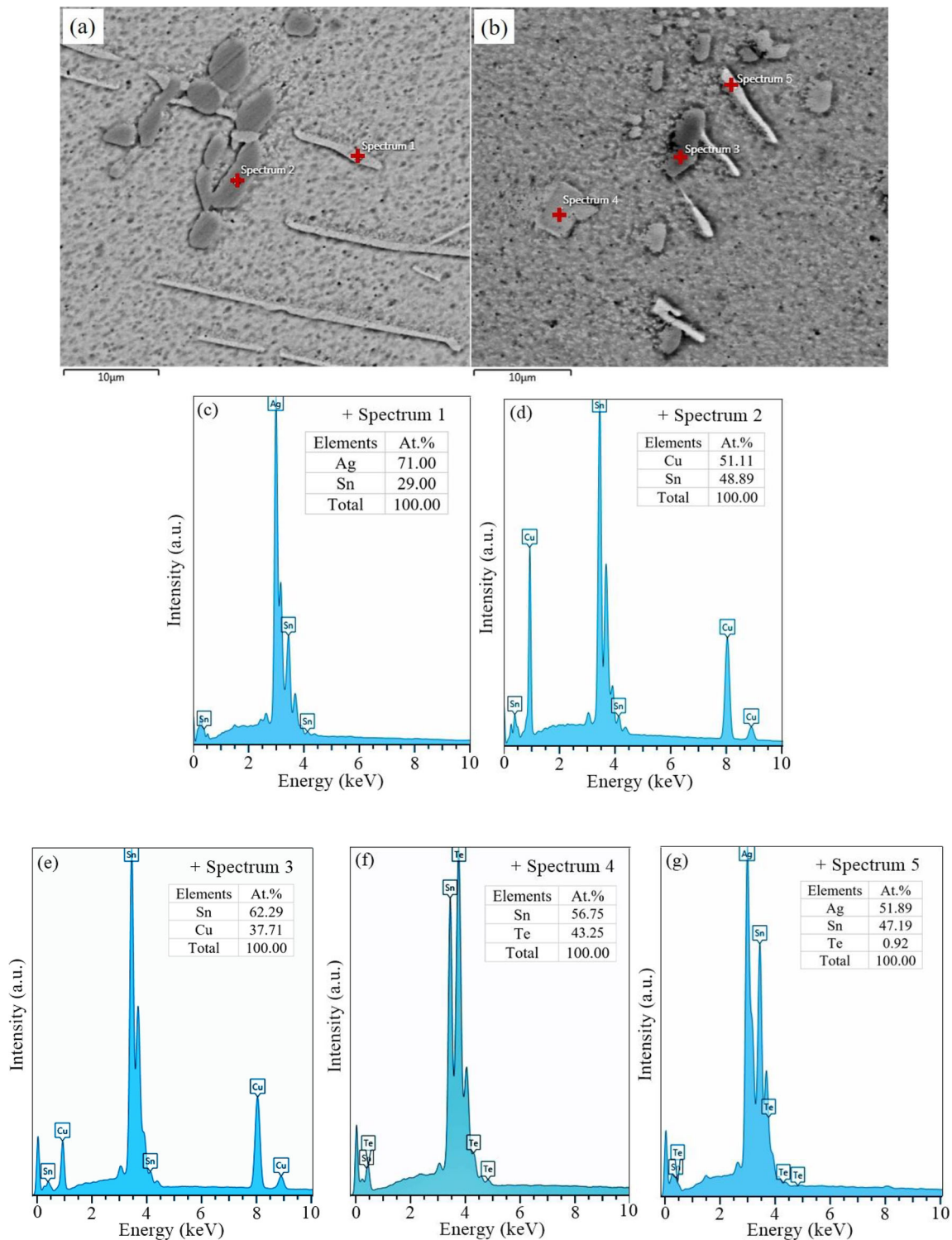
Fig. 4 SEM micrographs are of **a** SAC105 and **b** SAC105-1.5Te. Both alloys were analyzed by EDS. SAC105 presented **c** an Ag_3Sn IMC, and **d** a Cu_6Sn_5 IMC. SAC105-1.5Te presented **e** a Cu_6Sn_5 IMC, **f** an SnTe IMC, and **g** an Ag_3Sn IMC

Table 1 Phase compositions of solder alloys (at.%) identified by EDS analysis

Spectrum No	Sn	Ag	Cu	Te
1	29.00	71.00	–	–
2	48.89	–	51.11	–
3	62.29	–	37.71	–
4	56.75	–	–	43.25
5	47.19	51.89	–	0.92

solder. These findings were consistent with observations of the microstructures of SAC105-0.5Te, SAC105-1.0Te, and SAC105-1.5Te (Fig. 2). The melting, solidus, and liquidus temperatures and pasty range of the solder alloys were summarized in Table 3.
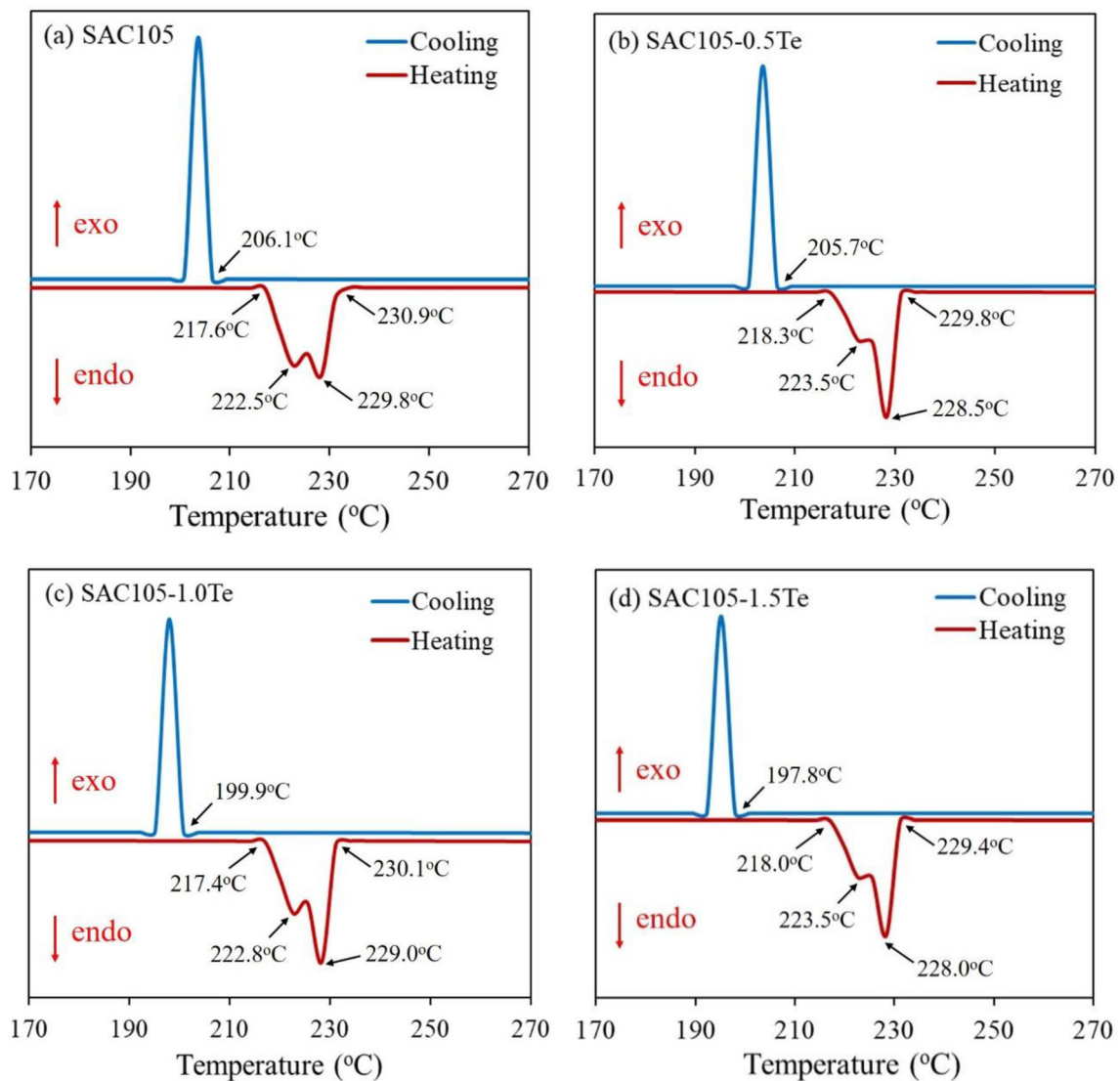

Fig. 5 DSC heating and cooling curves of **a** SAC105, **b** SAC105-0.5Te, **c** SAC105-1.0Te, and **d** SAC105-1.5Te solder alloys

Table 2 The undercooling of the studied solder alloys was calculated from the DSC heating and cooling curves

Solder alloy	$(T_{onset}, °C)$ Heating	$(T_{onset}, °C)$ Cooling	Undercooling (°C) $(T_{heating} - T_{cooling})$
SAC105	217.6	206.1	11.5
SAC105-0.5Te	218.3	205.7	12.6
SAC105-1.0Te	217.4	199.9	17.4
SAC105-1.5Te	218.0	197.8	20.1

Table 3 Data from the heating curves show the melting temperature (T_m), solidus temperature (T_{onset}), liquidus temperature (T_{end}), and pasty range of the studied solder alloys

Solder alloy	T_{m1} (°C)	T_{m2} (°C)	T_{onset} (°C)	T_{end} (°C)	Pasty range (°C) $(T_{end} - T_{onset})$
SAC105	222.5	229.8	217.6	230.9	13.3
SAC105-0.5Te	223.5	228.5	218.3	229.8	11.4
SAC105-1.0Te	222.8	229.0	217.4	230.1	12.7
SAC105-1.5Te	223.5	228.0	218.0	229.4	11.3

3.3 Mechanical properties

All the solder alloys displayed elastic and plastic deformation behavior before fracture (Fig. 6a–d). The addition of Te affected the YS, UTS, and elongation (%EL) of the solder alloy. The YS increased from 18.3 for SAC105 to 25.5 MPa for SAC105-0.5Te. UTS increased from 27.9 for SAC105 to 41.9 MPa for SAC105-0.5Te. %EL decreased from 32.0% for SAC105 to 16.3% for SAC105-0.5Te (Fig. 6e). These differences were due to differences in the microstructures of the alloys. The increased strength of the solder alloy was mainly derived from second-phase strengthening due to the formation of SnTe IMC particles in the solder matrix [17, 18]. Moreover, the addition of more than 0.5% Te tended to decrease the YS and UTS of the solder alloy by coarsening the microstructure (Fig. 2c–d). The hardness tests showed that only slight increases in hardness were obtained with the addition of Te (Fig. 6f), which were results of the formation of SnTe IMC particles in the solder matrix. The mechanical properties of the solder alloys were summarized in Table 4. Following tensile testing, the fracture morphologies of the solder alloys were analyzed by SEM. The fracture surface of the SAC105 solder alloy showed a heavily dimpled morphology, suggesting a plastic deformation prior to fracture, and a ductile fracture mechanism (Fig. 7a). All the SAC105 solder alloys containing Te exhibited a mixed ductile and brittle fracture behavior. The fracture surface showed dimples and cleavage planes, indicating the occurrence of both ductile and brittle fracture mechanisms (Fig. 7b–d). The changes in fracture mechanism were consistent with the ductility of the solder alloys indicated by tensile testing.

3.4 Wettability

The SAC105, SAC105-0.5Te, SAC105-1.0Te, and SAC105-1.5Te solder alloys all spread out on the Cu substrate and formed a clear wetting ring (Fig. 8a–d). The wettability of the solder alloys was evaluated from the spreading area of the solder and the contact angle ($θ$) formed between the solder and the substrate (Fig. 9). The spreading area of the solders containing Te were larger than the spreading area of the SAC105 solder. The spreading area of SAC105-0.5Te was approximately 31.5 mm^2, or 21.6% larger than that of the SAC105 solder (Fig. 9a). The contact angles between the Cu substrate and the reflowed samples containing Te were smaller than the contact angle between the SAC105 reflowed sample and the substrate (Fig. 9b). The contact angles of the SAC105-0.5Te, SAC105-1.0Te, and SAC105-1.5Te reflowed samples were 36.6°, 45.9°, and 45.1°, respectively, whereas the contact angle of the SAC105 reflowed sample was 52.3 ± 0.3 (Table 5). The contact angles
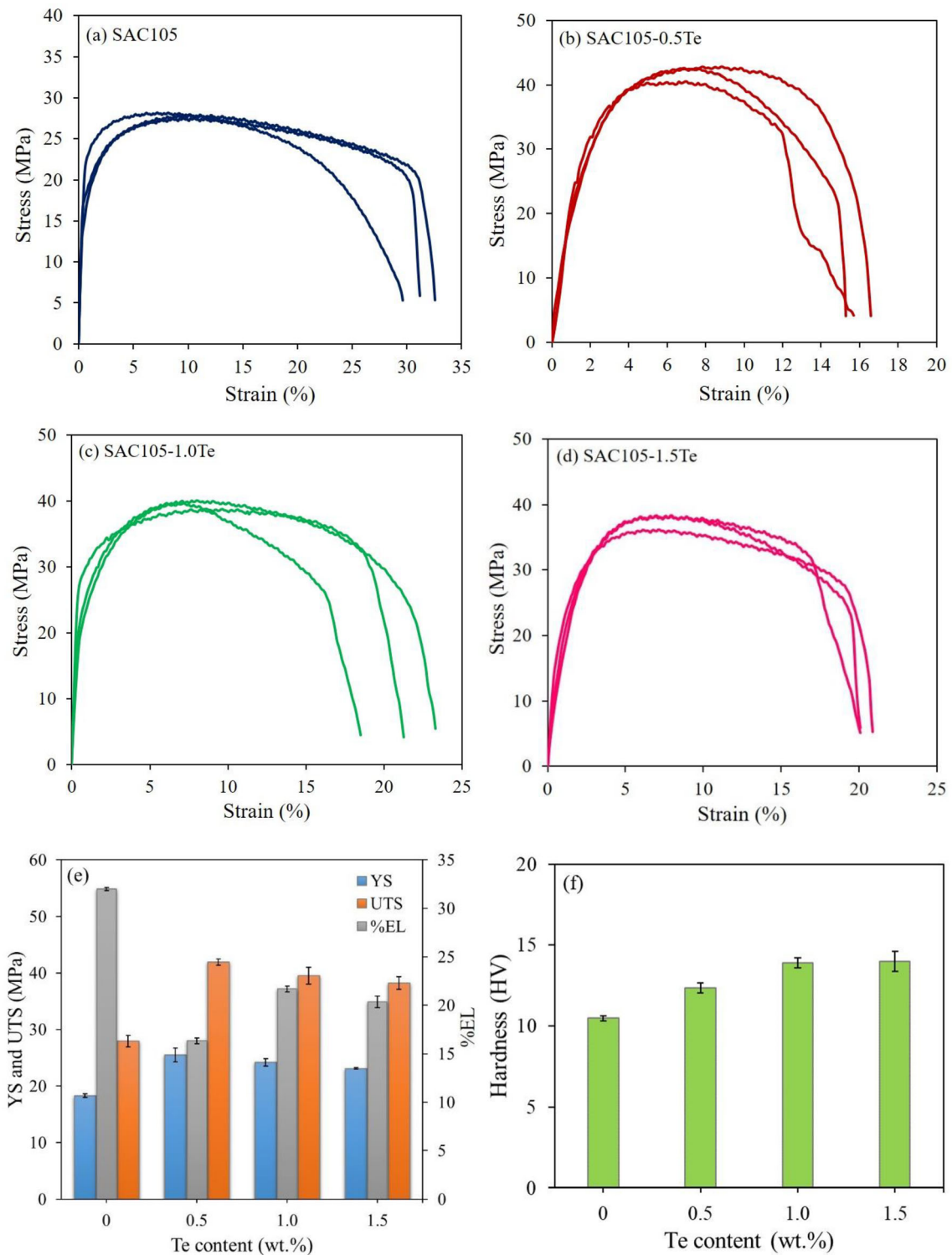
Fig. 6 The stress–strain curves are of **a** SAC105, **b** SAC105-0.5Te, **c** SAC105-1.0Te, and **d** SAC105-1.5Te solder alloys. The bar charts show **e** YS-UTS-%EL and **f** hardness of the same alloys, identified by tellurium content

Table 4 The yield strength (YS), ultimate tensile strength UTS, elongation (%EL) and hardness of the solder alloys

Solder alloy	Mechanical properties			
	YS (MPa)	UTS (MPa)	%EL	Hardness (HV)
SAC105	18.3 ± 2.0	27.9 ± 0.3	32.0 ± 1.0	10.5 ± 0.2
SAC105-0.5Te	25.5 ± 1.3	41.9 ± 1.2	16.3 ± 0.6	12.4 ± 0.3
SAC105-1.0Te	24.2 ± 1.4	39.5 ± 0.6	21.7 ± 1.5	13.9 ± 0.3
SAC105-1.5Te	23.1 ± 1.0	38.2 ± 0.2	20.3 ± 1.2	14.0 ± 0.6
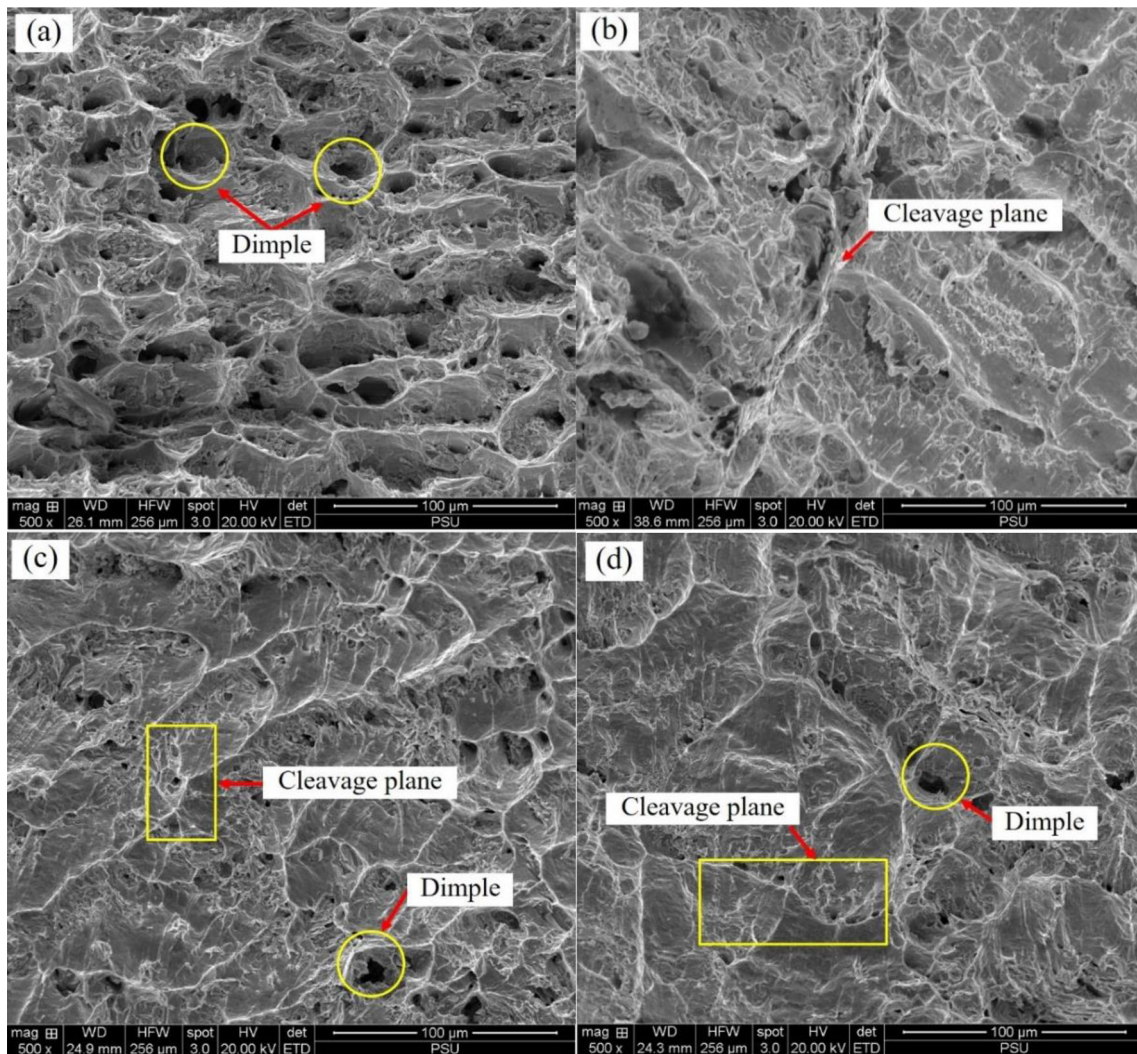
Fig. 7 The shown fracture surfaces are of **a** SAC105, **b** SAC105-0.5Te, **c** SAC105-1.0Te, and **d** SAC105-1.5Te after tensile testing to failure
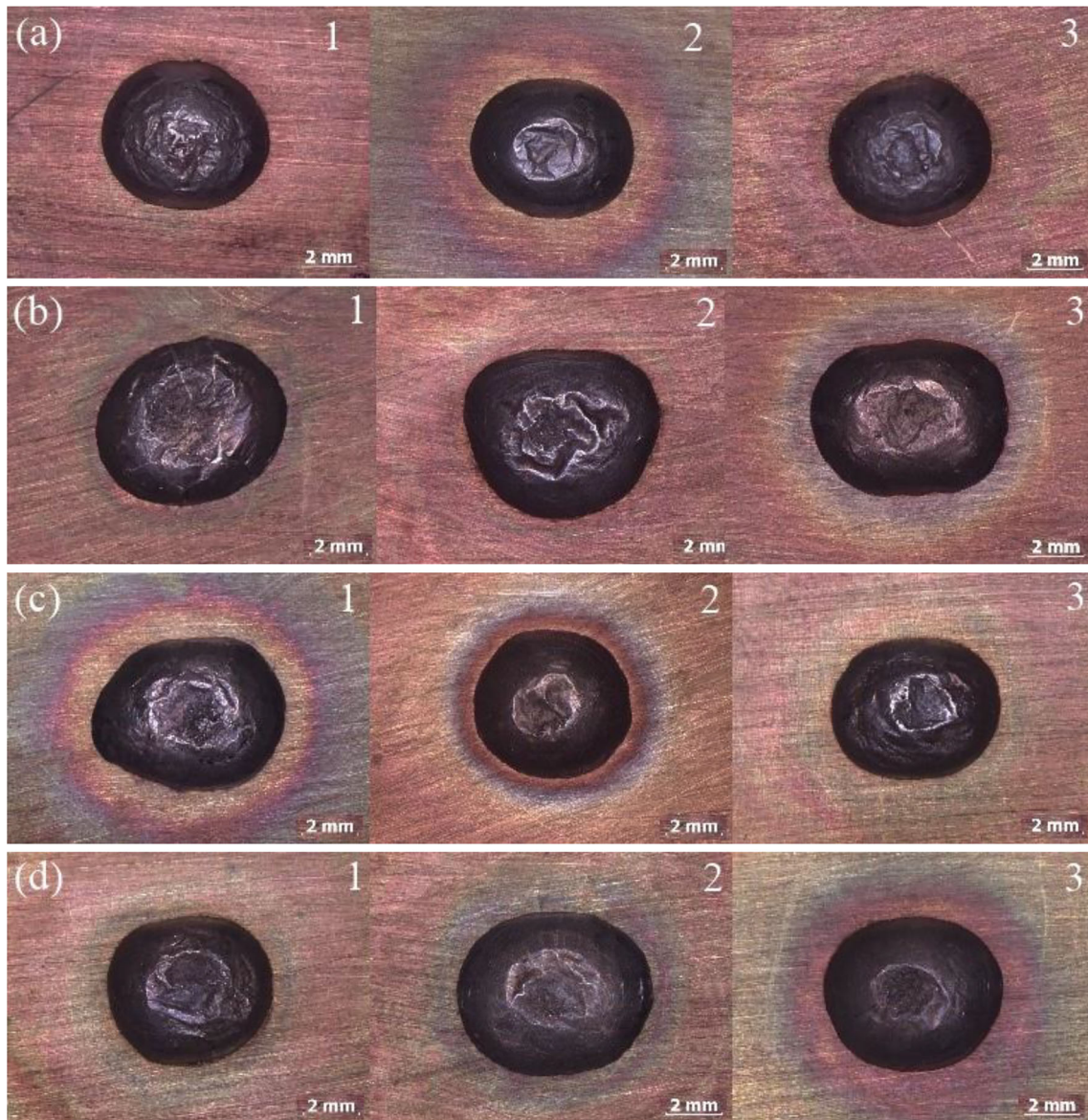
Fig. 8 Photographs of solder alloy samples after the spreading test show **a** SAC105/Cu, **b** SAC105-0.5Te/Cu, **c** SAC105-1.0Te/Cu, and **d** SAC105-1.5Te/Cu
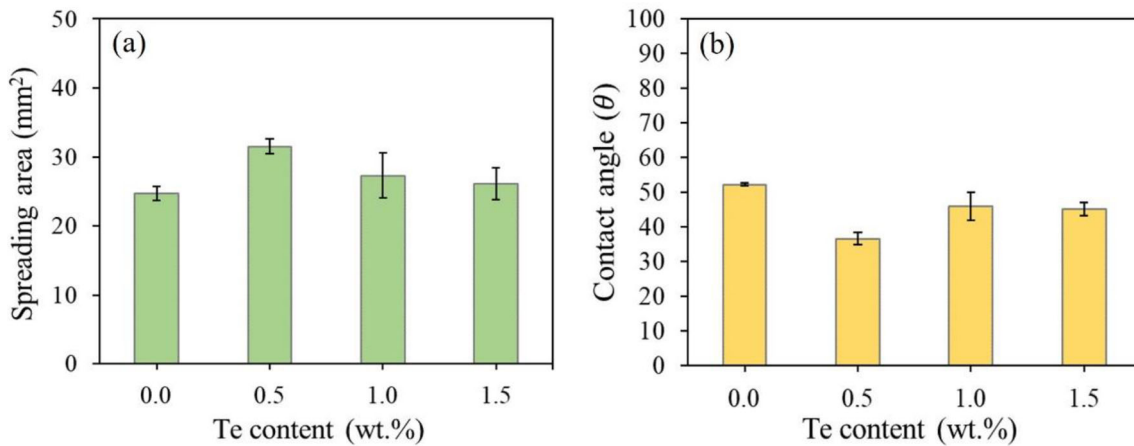
Fig. 9 The wettability of the studied solder alloys was assessed from **a** the spreading area, and **b** the contact angle formed between the solder and the Cu substrate

Table 5 The wettability of the solder alloys

Solder alloys	Contact angle (θ)	Spreading area (S_a, mm^2)
SAC105/Cu	52.3 ± 0.3	24.7 ± 0.9
SAC105-0.5Te/Cu	36.6 ± 1.7	31.5 ± 1.1
SAC105-1.0Te/Cu	45.9 ± 4.1	27.3 ± 3.2
SAC105-1.5Te/Cu	45.1 ± 1.9	26.1 ± 2.2

between the substrate and all the reflowed samples were within the wetting range denoted acceptable: $\theta > 0° < 30°$ is considered very good wetting; $\geq 30° < 40°$ good wetting; $\geq 40° < 55°$ acceptable wetting; $\geq 55° < 70°$ poor wetting; and $\theta \geq 70°$ very poor wetting [24]. Nevertheless, the addition of Te effectively improved the wettability of SAC105 solder. The spreading area and contact angle of the solder alloys were summarized in Table 5.

After the spreading test, the interfaces between the reflowed samples and the Cu substrate were examined by SEM. All the samples presented two IMC layers: a scallop-shaped Cu_6Sn_5 IMC layer and a thin Cu_3Sn IMC layer between the Cu_6Sn_5 IMC layer and the Cu substrate (Fig. 10). The formation of the IMC layers was due to the diffusion of Cu atoms from the substrate to the solder alloy, and the diffusion of Sn atoms from the solder alloy to the substrate [25, 26]. Cu_3Sn and Cu_6Sn_5 IMC phases were reported to form in Sn-Cu alloy during soldering at temperatures below 350 °C [27]. The addition of Te enabled the formation of SnTe IMC phases at the interface between the solder and the Cu_6Sn_5 IMC layer (Fig. 10b–d). EDS analysis of the IMC layers formed at the SAC105-1.5Te/Cu interface (Fig. 11a) confirmed the presence of an SnTe IMC phase (Fig. 11b),

a Cu_3Sn IMC layer (Fig. 11c), and a Cu_6Sn_5 IMC layer (Fig. 11d). The average thickness ($\bar{h}$) of IMC layers was determined from the SEM images in Fig. 10, and was calculated from the total area (A) and the length (L_x) of the IMC layers using image tool software [28]. The total thickness of the SAC105/Cu interface was about 6.76 μm. The addition of Te to SAC105 solder did not significantly affect the thickness of IMC layers in the reflowed samples. The total thickness of IMC layers was 6.50 μm at the SAC105-0.5Te/Cu and 7.11 μm at the SAC105-1.5Te/Cu. The average total thicknesses of Cu_6Sn_5 and Cu_3Sn IMC layers were summarized in Table 6.

4 Conclusion

The effect of Te addition on the microstructure, melting behavior, mechanical properties, and wettability of SAC105-xTe (x = 0, 0.5, 1.0, and 1.5) solder alloys was examined. The following main findings can be drawn:

1. The microstructure of SAC105 solder exhibited a primary β-Sn phase and an eutectic area with Ag_3Sn and Cu_6Sn_5 IMC phases. Increments of Te
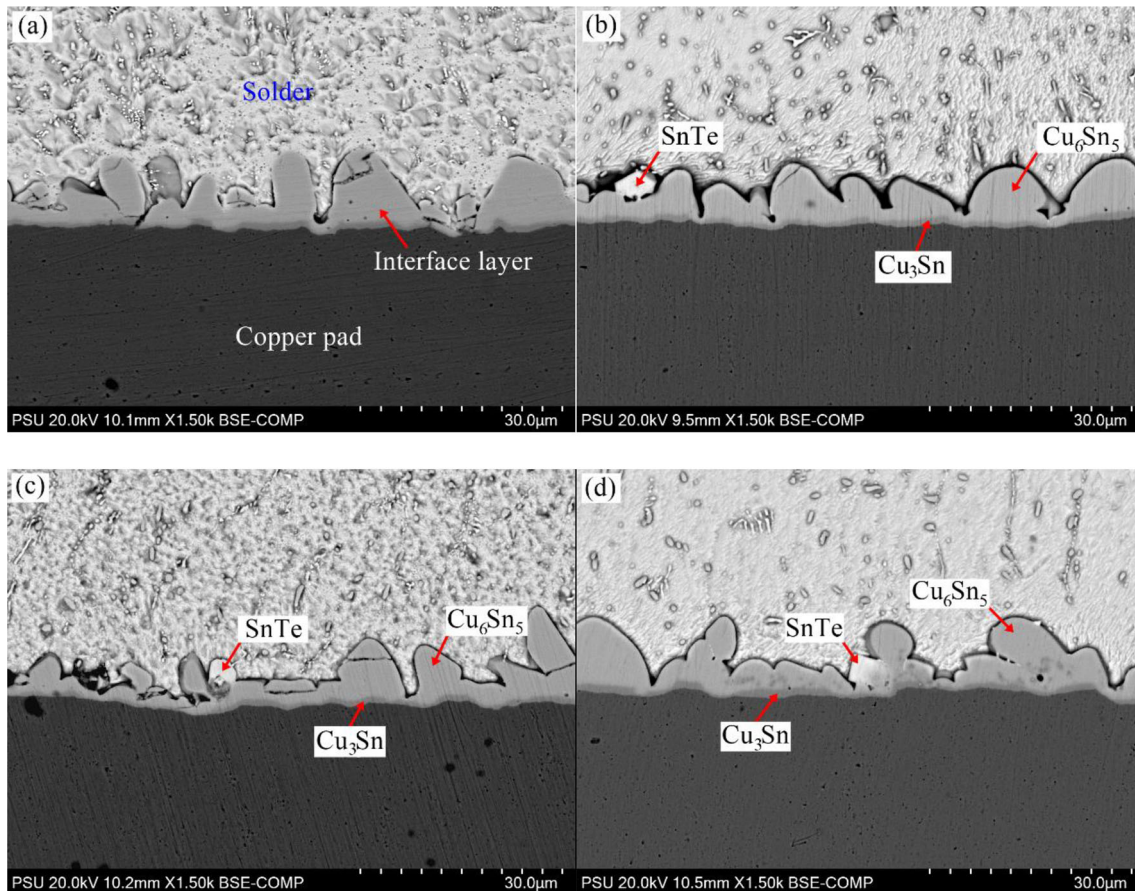
Fig. 10 SEM photographs show cross-sectional views of reflowed samples of **a** SAC105/Cu, **b** SAC105-0.5/Cu, **c** SAC105-1.0Te/Cu, and SAC105-1.5Te/Cu

content not only formed new SnTe IMC phases in the solder matrix but also made the β-Sn phase and IMC phases coarser.

2. The addition of Te slightly affected the melting temperature and pasty range but significantly affected the undercooling of SAC105 solder.

3. With the addition of Te, yield strength, ultimate tensile strength, and hardness increased significantly, and percent elongation decreased significantly due to the second-phase strengthening effect. When more than 0.5% Te was added to SAC105 solder, yield strength and ultimate tensile strength tended to decrease due to the coarsening of the microstructure.

4. The fracture surface of SAC105 solder displayed a ductile fracture mode, whereas a mixed ductile–brittle fracture mode developed in the SAC105-xTe solder alloys.

5. When Te was added to the SAC105 solder, the wettability of the solder alloys improved. The spreading area increased and the contact angle decreased, but the thickness of IMC layers formed between the solder and Cu substrate was not significantly affected.
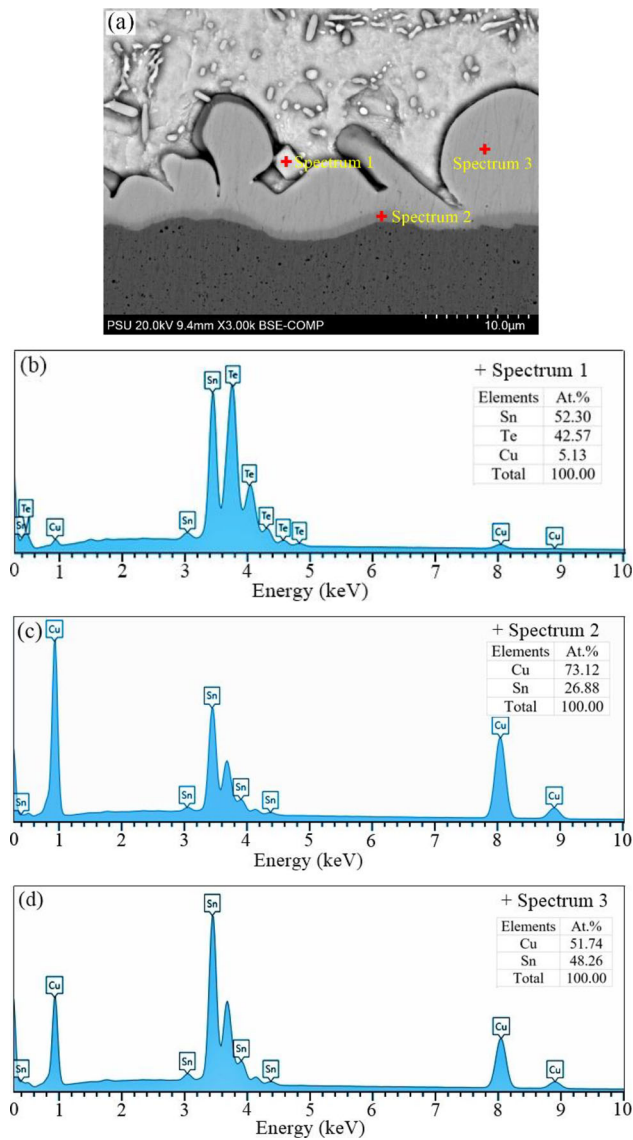
Fig. 11 The SEM image **a** shows an SAC105-1.5Te/Cu sample. EDS analysis of the sample detected **b** an SnTe IMC phase and interfacial layers of **c** a Cu$_3$Sn IMC, and **d** a Cu$_6$Sn$_5$ IMC

Author contributions

PS: methodology, investigation, visualization, software. PS: conceptualization, resources, data curation, validation, writing–original draft, writing–review & editing.

Data availability

The data and materials that support the findings of this study are available from the corresponding author upon reasonable request.

Declarations

Conflict of interest　The authors declare that they have no conflict of interest.

Table 6 Thickness of interfacial IMC layers of reflowed samples

Sample	Thickness of interfacial layer (µm), $\overline{h} = A/L_x$		
	Cu$_6$Sn$_5$	Cu$_3$Sn	Total
SAC105/Cu	5.78	0.98	6.76
SAC105-0.5Te/Cu	5.42	1.08	6.50
SAC105-1.0Te/Cu	4.75	0.83	5.58
SAC105-1.5Te/Cu	6.02	1.09	7.11

Ethical approval   This article does not contain any studies involving humans and animals performed by any of the authors.

References

1. F. Wang, M. O'Keefe, B. Brinkmeyer, J. Alloys Compd. **477**, 267–273 (2009). https://doi.org/10.1016/j.jallcom.2008.10.141

2. M. Zhao, L. Zhang, Z.Q. Liu, M.Y. Xiong, L. Sun, Sci. Technol. Adv. Mater. **20**, 421–444 (2019). https://doi.org/10.1080/14686996.2019.1591168

3. F. Yang, L. Zhang, Z.Q. Liu, S.J. Zhong, J. Ma, L. Bao, Adv. Mater. Sci. Eng. **2016**, 9265195 (2016). https://doi.org/10.1155/2016/9265195

4. W.R. Osorio, D.R. Leiva, L.C. Peixoto, L.R. Garcia, A. Garcia, J. Alloys Compd. **562**, 194–204 (2013). https://doi.org/10.1016/j.jallcom.2013.02.050

5. J. Sopousek, M. Palcut, E. Hodulova, J. Janovec, J. Electron. Mater. **39**, 312–317 (2010). https://doi.org/10.1007/s11664-009-1070-2

6. S.A. Belyakov, J. Xian, K. Sweatman, T. Nishimura, T. Akaiwa, C.M. Gourlay, J. Alloys Compd. **701**, 321–334 (2017). https://doi.org/10.1016/j.jallcom.2016.12.404

7. T. Luo, Z. Chen, A. Hu, M. Li, P. Li, Microelectron. Reliab. **53**, 2018–2029 (2013). https://doi.org/10.1016/j.microrel.2013.06.010

8. T. Kobayashi, K. Kobayashi, K. Mitsui, I. Shohji, Adv. Mater. Sci. Eng. **2018**, 1416942 (2018). https://doi.org/10.1155/2018/1416942

9. H. Wang, X. Hu, X. Jiang, Mater. Charact. **163**, 110287 (2020). https://doi.org/10.1016/j.matchar.2020.110287

10. X. Hu, T. Xu, L.M. Keer, Y. Li, X. Jiang, Mater. Sci. Eng. A **673**, 167–177 (2016). https://doi.org/10.1016/j.msea.2016.07.071

11. D.A.A. Shnawah, S.B.M. Said, M.F.M. Sabri, I.A. Badruddin, F.X. Che, J. Electron. Mater. **41**, 2631–2658 (2012). https://doi.org/10.1007/s11664-012-2145-z

12. Y. Chen, Z.C. Meng, L.Y. Gao, Z.Q. Liu, J. Mater. Sci.: Mater. Electron. **32**, 2172–2186 (2021). https://doi.org/10.1007/s10854-020-04982-4

13. D.A.A. Shnawah, S.B.M. Said, M.F.M. Sabri, I.A. Badruddin, F.X. Che, Mater. Sci. Eng. A **551**, 160–168 (2012). https://doi.org/10.1016/j.msea.2012.04.115

14. P.D. Pereira, J.E. Spinelli, A. Garcia, Mater. Des. **45**, 377–383 (2013). https://doi.org/10.1016/j.matdes.2012.09.016

15. M.H. Mahdavifard, M.F.M. Sabri, S.M. Said, S. Rozali, Microelectron. Eng. **208**, 29–38 (2019). https://doi.org/10.1016/j.mee.2019.01.011

16. A.A. El-Daly, A.E. Hammad, A. Fawzy, D.A. Nasrallh, Mater. Des. **43**, 40–49 (2013). https://doi.org/10.1016/j.matdes.2012.06.058

17. A.A. El-Daly, K.M. Zohdy, M.A. Abdo, N.A.M. Eid, J. Mater. Sci.: Mater. Electron. **30**, 13757–13767 (2019). https://doi.org/10.1007/s10854-019-01758-3

18. A.A. El-Daly, A.A. Ibrahim, M.A. Abdo, N.A.M. Eid, J. Mater. Sci.: Mater. Electron. **30**, 12937–12949 (2019). https://doi.org/10.1007/s10854-019-01656-8

19. P. Fima, T. Gancarz, J. Pstrus, A. Sypien, J. Mater. Eng. Perform. **21**, 595–598 (2012). https://doi.org/10.1007/s11665-012-0124-4

20. X. Chen, F. Xue, J. Zhou, Y. Yao, J. Alloys Compd. **633**, 377–383 (2015). https://doi.org/10.1016/j.jallcom.2015.01.219

21. A.E. Hammad, Mater. Des. **52**, 663–670 (2013). https://doi.org/10.1016/j.matdes.2013.05.102

22. C. Li, Y. Yan, T. Gao, G. Xu, Materials **13**, 4443 (2020). https://doi.org/10.3390/ma13194443

23. J.W. Elmer, E.D. Specht, M. Kumar, J. Elelctron. Mater. **39**, 273–282 (2010). https://doi.org/10.1007/s11664-010-1080-0

24. L. Zang, Z. Yuan, H. Xu, B. Xu, Appl. Surf. Sci. **257**, 4877–4884 (2011). https://doi.org/10.1016/j.apsusc.2010.12.131

25. P. Sebo, P. Svec, D. Janickovic, E. lllekova, Y. Plevachuk, Mater. Sci. Eng. A. **528**, 5955–5960 (2011). https://doi.org/10.1016/j.msea.2011.04.008

26. R. Rashidi, H. Naffakh-Moosavy, J. Mater. Res. Technol. **15**, 3321–3336 (2021). https://doi.org/10.1016/j.jmrt.2021.10.015

27. T. Laurila, V. Vuorinen, J.K. Kivilahti, Mater. Sci. Eng. R **49**, 1–60 (2005). https://doi.org/10.1016/j.mser.2005.03.001

28. R. Sayyadi, H. Naffakh-Moosavy, Sci. Rep. **9**, 8389 (2019). https://doi.org/10.1038/s41598-019-44758-3